



Interstellar Neutral Helium in the Heliosphere from *IBEX* Observations. VI. The He⁺ Density and the Ionization State in the Very Local Interstellar Matter

M. Bzowski¹ , A. Czechowski¹ , P. C. Frisch², S. A. Fuselier^{3,4}, A. Galli⁵ , J. Grygorczuk¹ , J. Heerikhuisen⁶ ,
M. A. Kubiak¹ , H. Kucharek⁷, D. J. McComas⁸ , E. Möbius⁷ , N. A. Schwadron⁷ , J. Slavin⁹ , J. M. Sokół¹ ,
P. Swaczyna^{1,8} , P. Wurz⁵ , and E. J. Zirnstein⁸

¹ Space Research Centre PAS (CBK PAN), Bartycka 18a, 00-716 Warsaw, Poland; bzowski@cbk.waw.pl

² University of Chicago, USA

³ Southwest Research Institute, San Antonio, TX, USA

⁴ University of Texas at San Antonio, San Antonio, TX, USA

⁵ University of Bern, Bern, Switzerland

⁶ University of Alabama in Huntsville, Huntsville, AL, USA

⁷ University of New Hampshire, Durham, NH, USA

⁸ Department of Astrophysical Sciences, Princeton University, Princeton, NJ, USA

⁹ Harvard-Smithsonian Center for Astrophysics, Cambridge, MA, USA

Received 2019 April 11; revised 2019 July 20; accepted 2019 July 22; published 2019 September 4

Abstract

Interstellar neutral gas atoms penetrate the heliopause and reach 1 au, where they are detected by *Interstellar Boundary Explorer* (*IBEX*). The flow of neutral interstellar helium through the perturbed interstellar plasma in the outer heliosheath (OHS) results in the creation of a secondary population of interstellar He atoms, the so-called Warm Breeze, due to charge exchange with perturbed ions. The secondary population brings the imprint of the OHS conditions to the *IBEX*-Lo instrument. Based on a global simulation of the heliosphere with measurement-based parameters and detailed kinetic simulation of the filtration of He in the OHS, we find the number density of the interstellar He⁺ population to be $(8.98 \pm 0.12) \times 10^{-3} \text{ cm}^{-3}$. With this, we obtain the absolute density of interstellar H⁺ as $5.4 \times 10^{-2} \text{ cm}^{-3}$ and that of electrons as $6.3 \times 10^{-2} \text{ cm}^{-3}$, with ionization degrees of 0.26 for H and 0.37 for He. The results agree with estimates of the parameters of the Very Local Interstellar Matter obtained from fitting the observed spectra of diffuse interstellar EUV and the soft X-ray background.

Key words: ISM: abundances – ISM: atoms – ISM: clouds – ISM: magnetic fields – local interstellar matter – Sun: heliosphere

1. Introduction

The Sun is traveling through a cloud of dilute (~ 0.25 nucleons cm^{-3}), warm (~ 7500 K), partly ionized, magnetized ($\sim 3 \mu\text{G}$) interstellar matter that is part of a larger cloud structure. This complex cloud is described in the literature either as a set of relatively small individual interstellar clouds (see, e.g., Redfield & Linsky 2008) or as a more sizable and complex structure with large-scale internal motions (Frisch et al. 2002; Gry & Jenkins 2014). It is located inside the Local Bubble (LB) of low-density ($\sim 10^{-3}$ nucleons cm^{-3}), hot (~ 1 MK), fully ionized plasma, which was most likely formed by overlapping superbubbles from recent nearby supernovae explosions (Frisch et al. 2011). The portion of interstellar matter that fills the immediate neighborhood of the Sun and thus is accessible to local observations will be referred to here as the Very Local Interstellar Matter (VLISM). The physical state of the matter within the VLISM is determined by elastic collisions, charge exchange and recombination processes, radiative cooling, ionization, and heating by EUV radiation from nearby stars and the LB, with a possible contribution from a nearby conductive interface between interstellar clouds and the LB (Slavin & Frisch 2008). Because of gradual absorption of the ionizing radiation inside the VLISM, the densities of the VLISM components, and consequently the local spectrum of the EUV radiation, vary with location in space.

The physical state, elemental composition, and ionization state of the VLISM are studied by fitting parameters of models to observed profiles of interstellar absorption lines and the

spectrum of the soft diffuse X-ray (McCammon et al. 1983; Bloch et al. 1986) and EUV (Vallerga et al. 2004) sky background. These are line-of-sight integrated observations of an inhomogeneous medium. Hence, investigating the physical state of the VLISM requires making parametric studies that consider cloud opacity (Slavin & Frisch 2008). Among the quantities that are challenging to obtain, but important for the VLISM physics, are absolute densities of the two main constituents of interstellar matter, hydrogen and helium. Their ionized fractions are especially important, because H⁺ does not produce absorption lines, and available observations of He⁺ lines are limited (Wolff et al. 1999). Even more challenging is investigating the magnetic field: this has been done on the scale of the global VLISM by analysis of the polarization of starlight by field-aligned grains of interstellar dust (Frisch et al. 2015).

Some of the VLISM parameters can be retrieved from direct sampling of interstellar neutral (ISN) atoms and their daughter products in the solar wind, i.e., pickup ions (PUIs), and thus they do not require global modeling of the heliosphere. They enable one to obtain the density of ISN H and He, their temperature, and the direction and speed of the Sun's motion through the VLISM.

Additional insight into the VLISM is obtained from comparing observations with predictions from global heliospheric modeling. The interaction of the solar wind and interstellar plasmas is modeled within a magnetohydrodynamic framework, coupled with a kinetic description of the plasma-neutral gas interaction (Baranov & Malama 1993; Pogorelov et al. 2009; Heerikhuisen et al. 2010). Results of this modeling

Table 1
Parameter Values Adopted in the Calculations

| Quantity | Magnitude | References |
|--|--|-------------------------|
| VLISM plasma mass density $\rho_{\text{pl,VLISM}}$ | 0.09 nucleons $\text{cm}^{-3\text{a}}$ | Zir2016 |
| VLISM neutral H density $n_{\text{H,VLISM}}$ | 0.154 $\text{cm}^{-3\text{a,b}}$ | Zir2016 |
| VLISM neutral He density $n_{\text{He,VLISM}}$ | 0.0150 ^{a,b} | Gloeckler et al. (2004) |
| VLISM temperature T_{VLISM} | 7500 K ^{a,c} | McComas et al. (2015b) |
| ISMF strength B_{ISMF} | 2.93 μG | Zir2016 |
| ISMF direction ($\lambda_{\text{ISMF}}, \beta_{\text{ISMF}}$) | (227°28, 34°62) ^{a,d} | Zir2016 |
| Sun's speed u_{VLISM} | 25.4 km s^{-1} | McComas et al. (2015b) |
| Sun's direction of motion ($\lambda_{\text{VLISM}}, \beta_{\text{VLISM}}$) | (255°7, 5°1) ^{a,d,e} | McComas et al. (2015b) |
| Solar wind density at 1 au n_{SW} | 5.74 cm^{-3} | Zir2016 |
| Solar wind temperature at 1 au T_{SW} | 5.1×10^4 K | Zir2016 |
| Solar wind speed at 1 au v_{SW} | 450 km s^{-1} | Zir2016 |
| Radial magnetic field of solar wind at 1 au $B_{r,\text{SW}}$ | 37.5 μG | Zir2016 |

Notes.

^a Fixed value adopted in the simulations of ISN He in this paper.

^b Uncertainty given as $0.16 \pm 0.04 \text{ cm}^{-3}$ for the determination of ISN H by Bzowski et al. (2009), and $\pm 0.0015 \text{ cm}^{-3}$ for the determination of ISN He by Gloeckler et al. (2004).

^c Affects the initial condition for the production and loss balance Equation (4). The uncertainty given as 7440 ± 260 K for the determination by Bzowski et al. (2015), but Swaczyna et al. (2018) suggests 7700 ± 230 K and Schwadron et al. (2015) 8000 ± 1300 K.

^d The directions of u_{VLISM} and B_{ISMF} determine the orientation of the $B - V$ plane, and consequently their uncertainties contribute to the uncertainty of the transformation from the reference system of the global heliosphere simulation to the ecliptic coordinates. The uncertainties for the direction of B_{ISMF} are $\pm 0.08 \mu\text{G}$ in strength and ($\pm 0^\circ 69, \pm 0^\circ 45$) in (longitude, latitude). The strength of B_{ISMF} does not directly affect our simulations of ISN He, just the global heliosphere model.

^e The uncertainties for longitude, latitude of u_{VLISM} are at least ($\pm 0^\circ 5, 0^\circ 1$) and for speed $\pm 0.3 \text{ km s}^{-1}$ (Swaczyna et al. 2018), but Schwadron et al. (2015) gives uncertainties for (longitude, latitude) equal to ($\pm 1^\circ 4, \pm 0^\circ 3$) and speed $\pm 1.1 \text{ km s}^{-1}$. The uncertainties of the VLISM velocity vector components and of T_{VLISM} are strongly correlated with each other.

provide predictions for various observable quantities, including the heliopause distance, plasma density, and magnetic field at the *Voyager* spacecraft, as well as the size and location of the *Interstellar Boundary Explorer* (*IBEX*) Ribbon.

The flux of ISN He atoms observed by the *IBEX*-Lo instrument (Fuselier et al. 2009; Möbius et al. 2009b) on board the *IBEX* mission (McComas et al. 2009) was resolved into the primary (Möbius et al. 2009a) and secondary (Kubiak et al. 2014) ISN populations. The secondary population is expected from heliospheric models (Baranov & Malama 1993) as a result of charge exchange between the plasma flowing by the heliopause and the unperturbed neutral gas in the outer heliosheath (OHS), i.e., the region ahead of the heliosphere where interstellar matter adapts to flow past the heliopause. For He, the dominant reaction is charge exchange between ISN He atoms and He^+ ions (Bzowski et al. 2012). Bzowski et al. (2017, hereafter Bz2017) simulated the ISN He signal observed by *IBEX* accounting for this charge exchange process in the OHS. They showed that the simulated signal is sensitive to the conditions in the OHS and VLISM, and to the plasma density and magnetic field vector among others.

Here, we constrain the absolute densities of the H^+ and He^+ components of the VLISM by fitting the ISN He signal observed by *IBEX* using the model from Bz2017 in conjunction with the global model of the heliosphere from Zirnstein et al. (2016, hereafter Zir2016). Observations and data selections are presented in Section 2. Simulation of the *IBEX* signal is described in Section 3, and the choice of parameter values used in the global heliospheric modeling performed for this study is discussed in Section 4 and presented in Table 1. The method used to obtain the He^+ densities is discussed in Section 5, and the VLISM parameters obtained are shown in Section 6 and Table 2. Discussion of the conclusions on the physical state of the VLISM concludes the paper.

Table 2
VLISM Parameter Values

| Quantity | Magnitude |
|--|--|
| He^+ number density n_{He^+} | $(8.98 \pm 0.12) \times 10^{-3} \text{ cm}^{-3}$ |
| Proton number density n_{H^+} | $5.41 \times 10^{-2} \text{ cm}^{-3}$ |
| Electron number density n_e | $6.30 \times 10^{-2} \text{ cm}^{-3}$ |
| Hydrogen ionization degree X_{H} | 0.26 ^a |
| Helium ionization degree X_{He} | 0.37 |

Note.

^a For $n_{\text{H}} = 0.154 \text{ cm}^{-3}$, adopted by Zir2016. If $n_{\text{H}} = 0.16 \text{ cm}^{-3}$ is adopted as measured by Bzowski et al. (2009), then this yields $X_{\text{H}} = 0.25$, which is very close to the previous value

2. Observations and Data Selection

The organization of the ISN gas sampling by *IBEX*-Lo was presented in detail by Möbius et al. (2009b, 2012, 2015), and here we only recall the most important aspects. *IBEX* is a spin-stabilized spacecraft orbiting the Earth in a highly elongated orbit with an apogee up to ~ 50 Earth radii. The spin axis of the spacecraft never points farther than $\sim 7^\circ$ from the Sun. The optical axis of the *IBEX*-Lo instrument is perpendicular to the spin axis. The atom detection events are accumulated in time so that they correspond to 6° bins of the spacecraft spin angle. For this study, we used the counting rate registered in energy step 2 (ESA 2) of *IBEX*-Lo in each of the spin angle bins, averaged over the time intervals regarded as free from magnetospheric and solar wind contamination (Galli et al. 2015, 2016). *IBEX* ISN observations are carried out between November and March each year.

The data we use here are from the same observation seasons as those used by Kubiak et al. (2016, Ku2016) to facilitate comparisons. Following these authors, we adopted counts from *IBEX*-Lo ESA 2, in the spin angle range from 216° to 318° ,

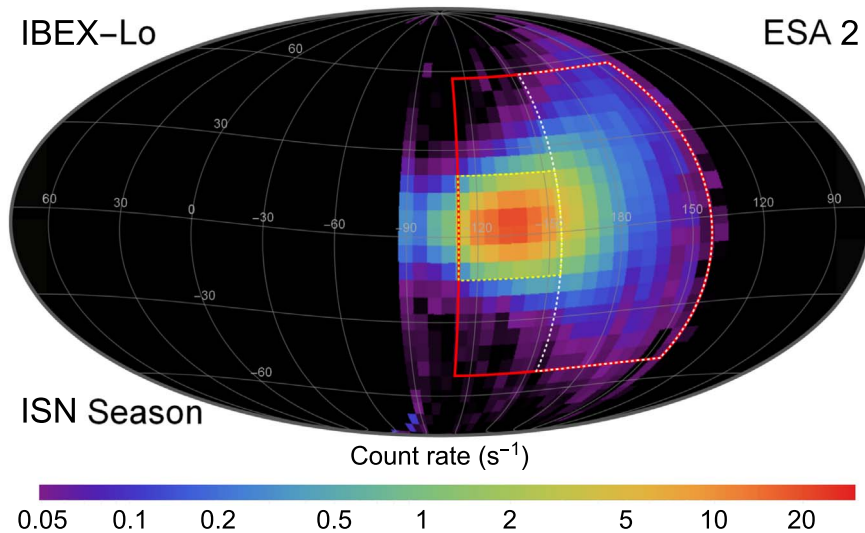


Figure 1. Sky map of the observed *IBEX*-Lo count rates from energy step ESA 2 used for analysis, averaged over the ISN observation seasons 2010–2014 (color-coded). The contours mark the data ranges used by Bzowski et al. (2015) to derive the ISN He parameters (yellow), by Ku2016 to derive the parameters of the secondary population of ISN He in the two-Maxwellian approximation (white), and in this work to derive interstellar He⁺ density in the VLISM (red).

collected during the observation seasons 2010–2014. Ku2016 restricted the data to the *IBEX* orbits where the signal from the secondary population (Warm Breeze) dominated (which corresponds to the range of ecliptic longitudes of *IBEX* spin axis 235°–295°). We use the yearly intervals corresponding to both the Warm Breeze and the primary ISN He signal, selecting the data based on an improved list of “good observation times” after Galli et al. (2016). We took orbits with both the Warm Breeze and the primary ISN signal because in our signal synthesis method we simulate both populations simultaneously, without differentiating between them. We cut off the portion of the data taken for spin axis longitudes greater than $\sim 335^\circ$ to avoid a contribution to the signal from ISN H (Swaczyna et al. 2018; Galli et al. 2019). As a consequence, we have significantly more data points (1422) than used by Bzowski et al. (2015) and Ku2016 (972). A comparison of the data range used by these studies and in this one is shown in Figure 1. The data we used are available in *IBEX* data release 12 at <http://ibex.swri.edu/researchers/publicdata.shtml>.

3. *IBEX* Signal Simulation

The signal simulation process is similar to that used by Bz2017. First, a global model of the heliosphere is run to provide the heliopause location and the plasma flow in the OHS. Subsequently, the observed signal is synthesized by integrating the contributions to the observed flux from individual He atoms. The statistical weights for these atoms are obtained from solutions of the production and loss balance equation. This equation is solved along the atom trajectories from the unperturbed interstellar medium through the OHS down to *IBEX* at 1 au.

We have verified that the region in the sky where atoms reaching *IBEX*-Lo penetrate the heliopause is oval-like, centered on the direction of inflow of the Warm Breeze (the secondary ISN He) found by Ku2016, and extends approximately $\pm 60^\circ$ in longitude and latitude (see Figure 2 here and Figure 7 in Bz2017). This is the region in the OHS ballistically connected to the *IBEX*-Lo instrument. This implies that predictions of any heliospheric model outside this region do not affect our results.

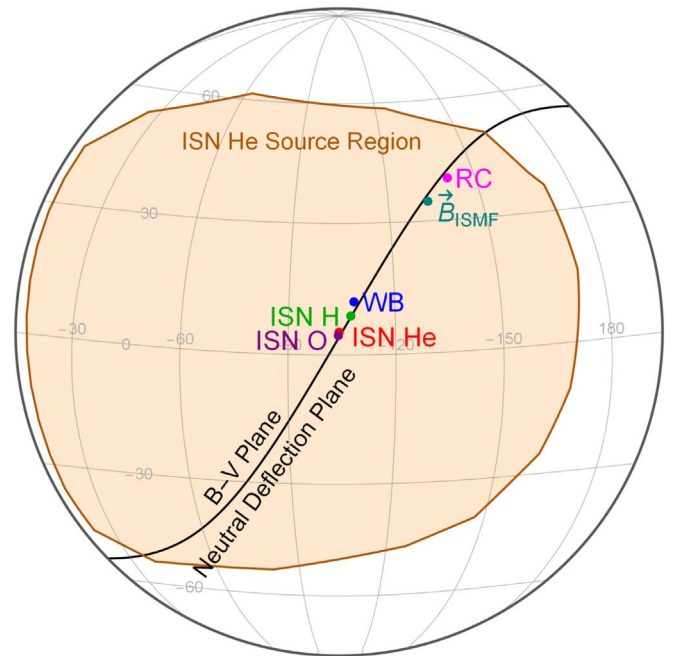


Figure 2. The geometry of the Sun’s motion through the VLISM, the ISMF vector (\mathbf{B}_{ISMF}), the Ribbon center (RC), and the secondary populations of ISN gas (“the Warm Breeze,” WB), projected on the sky. The direction of the Sun’s motion through the VLISM and its uncertainty as obtained by Bzowski et al. (2015) are marked by ISN He. Also shown is the direction of ISN O (Schwadron et al. 2016). The inflow direction of ISN H (Lallement et al. 2005) corresponds to a superposition of the primary and secondary populations. The average direction of RC is adopted following Funsten et al. (2013), and that of the unperturbed ISMF is adopted from Zir2016. The black line marks the neutral deflection plane (NDP) obtained by fitting the directions of ISN He, ISN H, and WB. The $B - V$ plane used in the calculations includes the directions of ISN He and \mathbf{B}_{ISMF} . The brown-shaded region is the projection on the sky of the locations at the heliopause where the He sampled by *IBEX*-Lo enters the heliosphere.

3.1. Boundary Conditions for ISN He

In the inertial reference system co-moving with the Sun, interstellar matter is inflowing on the heliosphere with the velocity $\mathbf{u}_{\text{VLISM}}$. The distribution function of ISN He in the unperturbed VLISM far ahead of the heliosphere is assumed to

be the Maxwell–Boltzmann distribution:

$$f_{\text{He}_{\text{VLISM}}}(\mathbf{v}) = n_{\text{He}_{\text{VLISM}}} \left(\frac{m_{\text{He}}}{2\pi k_{\text{B}} T_{\text{VLISM}}} \right)^{3/2} \times \exp \left[-\frac{m_{\text{He}}(\mathbf{v} - \mathbf{u}_{\text{VLISM}})^2}{2k_{\text{B}} T_{\text{VLISM}}} \right], \quad (1)$$

where \mathbf{v} is the velocity vector of an individual atom, the density of ISN He is $n_{\text{He}_{\text{VLISM}}}$, and $(2k_{\text{B}} T_{\text{VLISM}}/m_{\text{He}})^{1/2} = u_{\text{T,VLISM}}$ is the thermal speed of He in the VLISM for the temperature T_{VLISM} . This definition corresponds to Equation (6) in [Bz2017](#); note that [Bz2017](#) has a mistake in the denominator of the scaling factor in front of the exponent function.

3.2. He⁺ Ions in the OHS

The properties of the plasma in the OHS are adopted from the simulation of the interaction of the magnetized VLISM matter with the solar wind carried out using the Huntsville global MHD model of the heliosphere ([Heerikhuisen & Pogorelov 2010](#)) with simulation parameters identical to those found by [Zir2016](#) (see Table 1). This model uses proton plasma in the OHS and neglects all heavy ion components, including He⁺. In reality, He⁺ ions contribute significantly to the ram pressure because they have a mass ~ 4 times larger and a typical He-to-H number ratio in the astrophysical plasma is of the order of 0.1. Here, we interpret the plasma flow obtained in the model as a sum of a co-moving mixture of H⁺ and He⁺ ions. Moreover, the ratio of these two components is assumed constant throughout the OHS. Consequently, the density of He⁺ ions in the OHS is

$$n_{\text{He}_{\text{OHS}}^+}(\mathbf{r}) = n_{\text{He}_{\text{VLISM}}^+} \frac{\rho_{\text{pl}_{\text{OHS}}}(\mathbf{r})}{\rho_{\text{pl}_{\text{VLISM}}}}, \quad (2)$$

where $\rho_{\text{pl}_{\text{OHS}}}(\mathbf{r})$ is the assumed plasma density in the OHS from the global model, $\rho_{\text{pl}_{\text{VLISM}}}$ is the plasma density in the unperturbed VLISM, and $n_{\text{He}_{\text{VLISM}}^+}$ is the sought He⁺ density in the unperturbed VLISM. Further, we assume for H⁺ and He⁺ ions the same plasma flow $\mathbf{u}_{\text{OHS}}(\mathbf{r})$ and temperature $T_{\text{OHS}}(\mathbf{r})$, resulting from the global model. The plasma parameters in the OHS are interpolated between the grid nodes.

The distribution function of He⁺ ions in the OHS $f_{\text{He}_{\text{OHS}}^+}$ is assumed to be Maxwell–Boltzmann:

$$f_{\text{He}_{\text{OHS}}^+}(\mathbf{r}, \mathbf{v}) = n_{\text{He}_{\text{OHS}}^+}(\mathbf{r}) \left(\frac{m_{\text{He}}}{2\pi k_{\text{B}} T_{\text{OHS}}(\mathbf{r})} \right)^{3/2} \times \exp \left[-\frac{m_{\text{He}}(\mathbf{v} - \mathbf{u}_{\text{OHS}}(\mathbf{r}))^2}{2k_{\text{B}} T_{\text{OHS}}(\mathbf{r})} \right], \quad (3)$$

where m_{He} is the mass of He⁺ ion.

3.3. Statistical Weights of ISN He

The calculation of the statistical weights presented in this section was done exactly as in [Bz2017](#). Here, we present a description of this process that, in our opinion, better highlights the suitability of this method to obtain the absolute density of ISN He⁺.

The quantity used to calculate the signal is the statistical weight $\omega_{\text{loc}} = \omega(\mathbf{r}_{\text{loc}}, \mathbf{v}_{\text{loc}})$ at the location \mathbf{r}_{loc} where an atom moving with velocity \mathbf{v}_{loc} is detected. This quantity is obtained from numerical solution of the equation of production and loss balance (4) for He atoms on the trajectory s defined by the state vector of the atom at the detector $\mathbf{q}_{\text{stat}} = (\mathbf{r}_{\text{loc}}, \mathbf{v}_{\text{loc}})$. Since the atom motion is purely Keplerian (hyperbolic trajectory), the atom orbit s is uniquely determined by \mathbf{q}_{stat} . Therefore, any other state vector in this orbit $\mathbf{q}_s(t)$ can be obtained at any time. The relation between time and true anomaly (i.e., the heliocentric angle between the perihelion point of the orbit and the actual location of the atom in the orbit) is given by the hyperbolic Kepler equation.

The production and loss balance equation is defined as follows:

$$\frac{d\omega(t)}{dt} = \beta_{\text{pr}}(\mathbf{r}_s(t), \mathbf{v}_s(t)) f_{\text{He}_{\text{OHS}}^+}(\mathbf{r}_s(t), \mathbf{v}_s(t)) - \beta_{\text{loss}}(\mathbf{r}_s(t), \mathbf{v}_s(t)) \omega(t), \quad (4)$$

where $\beta_{\text{pr}} f_{\text{He}_{\text{OHS}}^+}$ represents the production of new neutral He atoms from He⁺ ions in the OHS, and $\beta_{\text{loss}}\omega$ the losses of neutral He atoms due to charge exchange with He⁺ ions. Here, the distribution function of He⁺ ions is a separate factor from the production rate β_{pr} , though they were multiplied together in Equation (11) in [Bz2017](#). The production and loss balance Equation (4) is solved for each considered state vector \mathbf{q}_s .

The production rate β_{pr} in a given location within the OHS along the trajectory s is determined by the rate of the resonant charge exchange reaction between ambient He atoms and He⁺ ions:

$$\beta_{\text{pr}}(\mathbf{r}, \mathbf{v}) = n_{\text{He}_{\text{VLISM}}} u_{\text{rel}}^{\text{pr}} \sigma_{\text{cx}}(u_{\text{rel}}^{\text{pr}}), \quad (5)$$

$$u_{\text{rel}}^{\text{pr}} = u_{\text{rel}}(|\mathbf{v} - \mathbf{u}_{\text{VLISM}}|, u_{\text{T,VLISM}}), \quad (6)$$

where σ_{cx} is the reaction cross section, and the mean relative speed $u_{\text{rel}}^{\text{pr}}$ is between an ion traveling at \mathbf{v} and a Maxwell–Boltzmann population of the ambient He atoms with temperature T_{VLISM} , bulk velocity $\mathbf{u}_{\text{VLISM}}$, and density $n_{\text{He}_{\text{VLISM}}}$, which are assumed constant throughout the OHS in this equation. The reaction involves no momentum exchange between the collision partners. The mean relative speed is calculated as

$$u_{\text{rel}}(\Delta u, u_{\text{T}}) = \left[\left(\frac{\Delta u}{u_{\text{T}}} + \frac{u_{\text{T}}}{2\Delta u} \right) \text{erf} \left(\frac{\Delta u}{u_{\text{T}}} \right) + \frac{\exp(-\Delta u^2/u_{\text{T}}^2)}{\sqrt{\pi}} \right] u_{\text{T}}. \quad (7)$$

This formula appropriately weights the velocity of the impactor particle relative to the centroid of the target particles and their thermal speed. It has been used in a number of papers, including the original paper by [Fahr & Mueller \(1967\)](#), and importantly by [Heerikhuisen et al. \(2015\)](#) and [Zir2016](#) in their modeling of the heliosphere.

The loss rate β_{loss} of He atoms at a location on the trajectory s is proportional to the sum of photoionization and charge exchange ionization rates. The magnitude of the photoionization rate in the OHS is assumed to be constant in time and equal to $\beta_{\text{ph},0}(r_{\text{E}}/r)^2$, with $\beta_{\text{ph},0}$ equal to the helium photoionization

rate at $r_E = 1$ au, averaged over the solar cycle (approximately 10^{-7} s^{-1}). The losses via charge exchange are due to collisions between He atoms and He^+ ions from the ambient OHS plasma. Consequently, the loss term is given by

$$\beta_{\text{loss}}(\mathbf{r}, \mathbf{v}) = \beta_{\text{ph},0} \left(\frac{r_E}{r} \right)^2 + n_{\text{He}^+_{\text{OHS}}}(\mathbf{r}) u_{\text{rel}}^{\text{loss}} \sigma_{\text{cx}}(u_{\text{rel}}^{\text{loss}}), \quad (8)$$

$$u_{\text{rel}}^{\text{loss}} = u_{\text{rel}}(|\mathbf{v} - \mathbf{u}_{\text{OHS}}(\mathbf{r})|, u_{\text{T,OHS}}(\mathbf{r})), \quad (9)$$

where $u_{\text{T,OHS}}(\mathbf{r}) = (2k_B T_{\text{OHS}}(\mathbf{r})/m_{\text{He}})^{1/2}$. Note that for calculation of the loss rates, the density, flow velocity, and temperature of the ambient He^+ ion population are obtained from the global model of the heliosphere.

The solution of the production and loss balance equation starts at a limiting distance, adopted as $\text{LD} = 1000$ au from the Sun. First, based on the orbital parameters obtained from the state vector \mathbf{q}_{stat} at the detector location, the velocity $\mathbf{v}_s(t_{\text{LD}})$ at the limiting distance of the calculation is determined. Beyond this distance, all interstellar populations are assumed to be homogeneous in space and in collisional equilibrium. With that, the initial condition for Equation (4) ω_0 is defined as

$$\omega_0 = f_{\text{HeVLSISM}}(\mathbf{v}_s(t_{\text{LD}})), \quad (10)$$

with f_{HeVLSISM} defined in Equation (1). Note that, a priori, any reasonable form of f_{HeVLSISM} can be adopted, including, e.g., a kappa function, such as that used by Sokół et al. (2015a), but if so, then consequently both in the global simulation and in the calculation of the statistical weights. Moreover, since all terms in Equation (4) are proportional to the density of ISN He in the VLISM ($\omega, \beta_{\text{pr}} \propto n_{\text{HeVLSISM}}$), this density cannot be obtained from *IBEX* observations without relying on the absolute instrument calibration. However, only the loss rate and the distribution function of He^+ in the OHS are proportional to the density of He^+ ions ($\beta_{\text{loss}}, f_{\text{He}^+_{\text{OHS}}} \propto n_{\text{He}^+_{\text{VLSISM}}}$). Therefore, the absolute density of He^+ can be retrieved from comparison of statistical weights ω obtained for the atom orbits with different statistical weights ω_0 at the limiting distance LD. The result does not depend on the magnitude of the adopted density of ISN He in the unperturbed VLISM.

For the $\text{He}^+ + \text{He}$ charge exchange cross section, we used the formula from Barnett et al. (1990), adapted for low collision speeds of a few km s^{-1} (Equation (10) in Bz2017). We neglect the charge exchange between the He and H populations (neutral and ionized) because the cross sections for these reactions are ~ 250 times lower than those for the $\text{He}^+ + \text{He} \rightarrow \text{He} + \text{He}^+$ reaction for the low collision speeds ($\sim 5\text{--}50 \text{ km s}^{-1}$) characteristic of the charge exchange collisions in the OHS.

With the initial condition defined, Equation (4) is solved along the trajectory down to the detector. Solving this equation is done in two parts: first between the source region and the heliopause, i.e., within the OHS, and subsequently from the heliopause to the detector.

For the solution of Equation (4) within the OHS we assume a time-stationary situation. With this, Equation (4) is transformed so that the integration goes over the true anomaly angle θ , which becomes the independent variable: $dt = \frac{r^2}{L} d\theta$, where $L = |\mathbf{L}| = |\mathbf{r}_{\text{loc}} \times \mathbf{v}_{\text{loc}}|$ is the angular momentum per unit mass, constant over the atom orbit. Inside the heliopause, calculating the losses is carried out exactly as in our previous papers presenting analyses of *IBEX* ISN He observations: Bzowski et al. (2012, 2015), Kubiak et al. (2014, 2016), Swaczyna et al. (2018).

Ultimately, the solution returns the statistical weight ω_{loc} of a given atom at the detector, which can be regarded as the magnitude of the local distribution function of neutral He at the detector site for the atom state vector \mathbf{q}_s .

3.4. Integration with *IBEX-Lo* Response

The calculation scheme of the *IBEX-Lo* signal due to ISN He takes into account all important details of the data-taking procedure so that the simulated signal can be directly compared with the *IBEX-Lo* data product (Sokół et al. 2015b). In this paper, we precisely follow the approach described by these authors up to the point in the calculations where the magnitude of the local distribution function of ISN He for a given state vector of the atom at the detector is needed. There, the method is changed to that developed by Bz2017 and presented in detail in Sections 3.1–3.3.

4. Parameter Values for the Simulations

In this section we present the parameters used in the two-tier simulations performed to obtain the He^+ density in the VLISM and argue that they are supported by a strong observational foundation. The adopted parameter values were used consistently in the global simulation of the heliosphere and in the simulations used to derive the He^+ density in the VLISM. They are collected in Table 1.

4.1. VLISM Parameters

4.1.1. Sun's Velocity Vector and ISN Gas Temperature

The vector of the Sun's velocity relative to the VLISM and the VLISM temperature had been obtained from extensive analyses of direct-sampling observations of ISN He available from *Ulysses* (Witte 2004; Bzowski et al. 2014; Wood et al. 2015) and *IBEX* (Bzowski et al. 2015; McComas et al. 2015a, 2015b; Möbius et al. 2015; Schwadron et al. 2015). We adopted them following McComas et al. (2015b) to maintain homogeneity with Zir2016. The vector of the inflow velocity of ISN gas on the heliosphere, used in Equation (1), is given by $\mathbf{u}_{\text{VLSISM}} = -u_{\text{VLSISM}}(\cos \lambda_{\text{VLSISM}} \cos \beta_{\text{VLSISM}}, \sin \lambda_{\text{VLSISM}} \cos \beta_{\text{VLSISM}}, \sin \beta_{\text{VLSISM}})$. These parameters are independent of heliosphere models since they rely on atom ballistics and ionization losses, obtained from measurements of relevant solar factors (Section 4.2).

Alternatively, the velocity of the Sun's motion through the VLISM can be assessed from observations of the Doppler shifts of interstellar absorption lines visible in the spectra of nearby stars (Adams & Frisch 1977), using a method developed by Crutcher (1982). In this case, the result would be an average value over a distance of at least several parsecs. For our purpose, however, the value of the Sun's speed and the VLISM temperature must be determined precisely at the Sun's location.

4.1.2. Mass Density of Interstellar Plasma and Number Density of ISN H

The value of plasma mass density was chosen to provide the ram pressure needed, together with magnetic pressure, to obtain the heliopause distance in agreement with that found by *Voyager 1*: $\rho_{\text{pl,VLSISM}} = 0.09 \text{ nucleons cm}^{-3}$. This is the total mass density of the plasma, assumed to be composed of H^+ and He^+ ions. The expected contribution to the total mass density of the VLISM plasma from He^{++} and heavy ions is

negligible for the pressure balance (Slavin & Frisch 2008). This quantity is model-dependent, but the model used to derive it has been demonstrated to reproduce the target observable parameters (see details in Zir2016). This approach was qualitatively verified by measurement in situ of the total electron density in the region of compressed plasma beyond the heliopause by *Voyager 1* (Gurnett et al. 2013, 2015) as $\sim 0.09 \text{ cm}^{-3}$, in qualitative agreement with predictions of the Huntsville heliosphere simulation for this region, reported by Zir2016. Also the intensity of the draped magnetic field in the Huntsville model was compliant with the values measured by *Voyager* (Burlaga & Ness 2016).

The density of ISN H at the termination shock (TS) was determined using two independent methods. One of them is based on the magnitude of the slowdown of the solar wind inside TS due to mass- and momentum-loading from pickup of ISN H atoms ionized by charge exchange or photoionization (Isenberg 1986; Fahr & Ruciński 1999; Lee et al. 2009). This slowdown is proportional to the absolute density of ISN H at TS. Based on observations of *Voyager 2* and *Ulysses*, it was measured by Richardson (2008) to be $\sim 67 \text{ km s}^{-1}$. Using a one-dimensional MHD model of the slowdown, these authors determined the density of ISN H at TS as $0.09 \text{ atoms cm}^{-3}$.

The other method is based on the fact that the production rate of H^+ PUIs at the boundary of the ISN H cavity is linearly dependent on the TS density of ISN H, but depends very weakly on all other parameters, including the solar resonant radiation pressure and the velocity, temperature, and ionization rate of ISN H. The PUI production rate was measured by SWICS on *Ulysses* (Gloeckler & Geiss 2001), and based on this measurement and modeling of the PUI production rate, the ISN H density at TS was determined by Bzowski et al. (2008) to be $0.087 \pm 0.022 \text{ cm}^{-3}$, in excellent agreement with the value obtained from the slowdown of the solar wind. Kowalska-Leszczynska et al. (2018) independently supported this conclusion using better models of radiation pressure and ionization losses. Based on the findings of Richardson et al. (2008) and Bzowski et al. (2008), Bzowski et al. (2009) suggested that the ISN H number density at TS is $0.09 \pm 0.02 \text{ cm}^{-3}$, and the number density in the unperturbed VLISM is $0.16 \pm 0.04 \text{ atoms cm}^{-3}$. The number density of ISN H at TS is independent of global heliospheric modeling. The transition from the TS density to the density in the unperturbed VLISM is done by heliospheric modeling (e.g., Izmodenov et al. 2003a, 2003b), but the TS/VLISM ratio for n_{H} only weakly depends on the details of these models (Bzowski et al. 2008). In the global heliospheric simulation in our paper, we adopted the VLISM H density $n_{\text{H,VLISM}} = 0.154 \text{ atoms cm}^{-3}$, as in Zir2016, which is in agreement with the aforementioned determination.

4.1.3. Number Density of ISN He

The unperturbed density of ISN He was determined using several methods.

The PUI measurement by Gloeckler et al. (2004) was based on the ratio between the He^{++} in the core solar wind and He^{++} PUIs measured by SWICS on *Ulysses*, independently of the absolute calibration of the instrument. The He density was also determined from observations of the absolute flux of He^+ PUIs by SWICS, but in this case the absolute calibration had to be used. The results turned out to be in excellent agreement with

each other, and the density of ISN He from PUI measurements was reported as $0.0151 \pm 0.0015 \text{ atoms cm}^{-3}$.

Witte (2004) measured the absolute density of ISN He from observations of the absolute flux of ISN He sampled at *Ulysses* by the GAS instrument, and obtained $0.015 \pm 0.003 \text{ atoms cm}^{-3}$ using the absolute calibration of that instrument. Based on these measurements, Möbius et al. (2004) suggested that the absolute density of ISN He in the VLISM is equal to $0.0148 \pm 0.002 \text{ atoms cm}^{-3}$. Cummings et al. (2002) measured this density based on appropriately corrected anomalous cosmic-ray fluxes and obtained 0.017 ± 0.002 .

In this work, we have adopted the value obtained from the PUI and direct-sampling measurements: $n_{\text{He,VLISM}} = 0.0150 \pm 0.0015 \text{ atoms cm}^{-3}$ after Gloeckler et al. (2004) and Witte (2004).

4.1.4. Unperturbed Interstellar Magnetic Field (ISMF) Vector

The vector of unperturbed ISMF was determined based on measurements of starlight polarization on dust grains aligned with ISMF field lines and independently based on the center position and size of the *IBEX* Ribbon.

The measurement based on starlight polarization obviously does not depend on any heliospheric modeling but it provides the ISMF vector averaged over several dozen parsecs. Frisch et al. (2015) reported the direction of this field as $(\lambda_{\text{ISMF}}, \beta_{\text{ISMF}}) = (229^\circ.1, 41^\circ.1)$ with an uncertainty of 16° around this direction. The angle between this direction and the direction of the Sun's motion relative to the VLISM is $43^\circ.1$.

Grygorczuk et al. (2011), Heerikhuisen & Pogorelov (2011), and Zir2016 determined the unperturbed ISMF vector by fitting the position of the *IBEX* Ribbon center and its diameter under the hypothesis that the Ribbon is created due to the mechanism for secondary energetic neutral atom (ENA) emission in the OHS (Heerikhuisen et al. 2010). In this mechanism, the arc-like region of enhanced ENA emission marks in the sky the region where the ISMF draped in the OHS is perpendicular to the solar-radial direction: $\mathbf{B} \cdot \mathbf{r} = 0$.

Grygorczuk et al. (2011) and Heerikhuisen & Pogorelov (2011) adopted parameter grids with several combinations of the \mathbf{B}_{ISMF} field strength and the inclination of \mathbf{B}_{ISMF} to the ISN velocity $\mathbf{u}_{\text{VLISM}}$ and found that the best fitting parameter set is that with $\mathbf{B}_{\text{ISMF}} = 3 \mu\text{G}$ and the directions $(\lambda_{\text{ISMF}}, \beta_{\text{ISMF}}) = (225^\circ \pm 15^\circ, 35^\circ \pm 5^\circ)$ and $(222^\circ \pm 2^\circ, 41^\circ.5 \pm 2^\circ.5)$, respectively. The resulting angles between the \mathbf{B}_{ISMF} and $\mathbf{v}_{\text{VLISM}}$ vectors are $40^\circ.3$ and $47^\circ.2$, respectively.

Zir2016 used the aforementioned interstellar and solar wind parameters (except \mathbf{B}_{ISMF}) as input to the Huntsville model of the heliosphere. They sought the strength and direction of the ISMF for which the heliopause distance in the *Voyager 1* direction would match that observed, the direction and strength of the draped \mathbf{B} -field inside OHS would match those observed by *Voyager 1*, and the center and size of the Ribbon would be in agreement with observations of Funsten et al. (2013). They performed global simulations with different ISMF vectors, varying its strength between 2 and $4 \mu\text{G}$, and found that the best fitting results are obtained for $\mathbf{B}_{\text{ISMF}} = 2.93 \pm 0.08 \mu\text{G}$, directed toward $(\lambda_{\text{ISMF}}, \beta_{\text{ISMF}}) = (227^\circ.28 \pm 0^\circ.69, 34^\circ.62 \pm 0^\circ.45)$. The angle between this direction and the direction of $\mathbf{u}_{\text{VLISM}}$ is equal to $39^\circ.5$, which is in agreement with the aforementioned results.

The credibility of the ISMF vector thus obtained is further enhanced by the observation by Ku2016 that the secondary population of ISN He (dubbed the Warm Breeze) flows into the heliosphere from the direction $(\lambda_{\text{WB}}, \beta_{\text{WB}}) = (251^\circ.6, 12^\circ)$, i.e.,

within the plane defined by the $\mathbf{u}_{\text{VLISM}}$ and \mathbf{B}_{ISMF} vectors. State-of-the-art global heliospheric simulations (e.g., Pogorelov et al. 2008; Izmodenov & Alexashov 2015) suggest that the directions of the ISMF, the Sun’s motion, and the inflow of the secondary populations on the heliosphere should be co-planar. And indeed, such a geometry is implied by observations of ISN He, H, O (Schwadron et al. 2016), the secondary population of ISN He, the Ribbon center, and the direction of ISMF, as illustrated in Figure 2.

With this, we decided to adopt the \mathbf{B}_{ISMF} vector found by Zir2016 along with the other VLISM parameters they used in our analysis. The input VLISM parameter values are collected in Table 1.

4.2. Solar-side Conditions

The solar wind flux and magnetic field contribute to the pressure balance at the heliopause and thus define the shape of the heliosphere and the distance to the heliopause. Furthermore, the charge exchange and photoionization processes together with radiation pressure modify the distribution of ISN H density inside the TS and hence affect the flux of PUIs, which mediate the TS. Therefore, an appropriate model of the solar wind is essential for any global heliosphere model. Additionally, the solar EUV output is responsible for ionization of ISN He inside the TS, and thus for the ISN He signal observed by *IBEX*. Consequently, it is important to adopt realistic models of these factors in the global heliosphere modeling and in the model of the *IBEX* ISN He signal. A review of the solar conditions relevant for heliospheric studies was presented by Bzowski et al. (2013b).

4.2.1. Solar Wind Parameters

In the global simulations of the heliosphere that we used, the solar wind was assumed to be time-stationary and spherically symmetric. These simplifications are justified because the most important solar wind parameter for the global shape of the heliosphere is dynamic pressure, which is close to invariant with heliolatitude (McComas et al. 2008, 2013). For the location of the heliopause, time-variations within the supersonic solar wind are of minor importance, as argued by Zir2016. In the simulations used in this paper, the boundary conditions at 1 au were adopted following Zir2016: plasma density $\rho_{\text{SW}} = 5.74$ nucleons cm^{-3} , plasma temperature $T_{\text{SW}} = 51,000$ K, solar wind speed $v_{\text{SW}} = 450$ km s^{-1} , radial component of the frozen-in magnetic field $B_{r,\text{SW}} = 37.5$ μG . These conditions were advected to the inner boundary of the simulation at 10 au assuming adiabatic expansion. The numerical values were chosen to obtain the heliopause distance corresponding to the heliopause crossing by *Voyager 1* (Stone et al. 2013). The resulting model shows an agreement with the heliopause crossing distance from *Voyager 2* (Heerikhuisen et al. 2019). The choice of the solar wind parameters is in agreement with a reconstruction by Sokół et al. (2015a) based on in situ measurements (King & Papitashvili 2005) and remote-sensing observations of interplanetary scintillations (Tokumaru et al. 2015).

4.2.2. Ionization Rates by Solar EUV Radiation and Solar Wind Electron Impact

For modeling the signal due to ISN He observed by *IBEX*, we adopted an observation-based model of photoionization and

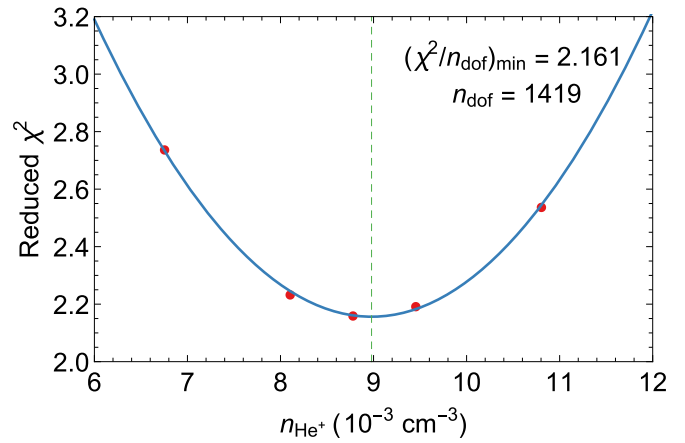


Figure 3. Reduced chi-squared values obtained for simulations of the signal carried out assuming various densities of He^+ in the VLISM. The red points show the results for the simulated values of n_{He^+} , and the blue line is the second-order polynomial fitted to the results. The polynomial minimum is marked with the green dashed bar.

electron-impact losses for He inside the heliopause from Bzowski et al. (2013a), extended by Sokół & Bzowski (2014) and Sokół et al. (2019). The dominant loss reaction is photoionization, supplemented by electron-impact ionization with the radial variation of the rate adopted from Bzowski et al. (2013a).

5. Parameter Fitting

Since practically all interstellar He in the VLISM is either neutral or singly ionized (Slavin & Frisch 2008) and other species contribute negligibly, we assumed that both in the unperturbed VLISM and in the OHS the plasma mass density $\rho_{\text{pl}} = (n_{\text{H}^+} + 4n_{\text{He}^+})m_{\text{nuc}}$, where m_{nuc} is nucleon mass and n_{H^+} , n_{He^+} are the number densities of H^+ and He^+ , respectively. With this, we calculated $n_{\text{He}^+_{\text{VLISM}}}$ by chi-squared fitting the ISN He signal observed by *IBEX* from 2010 to 2014 with varying $n_{\text{He}^+_{\text{VLISM}}}$ while keeping $\rho_{\text{pl}_{\text{VLISM}}}$ unchanged.

The observed signal was simulated for five values of $n_{\text{He}^+_{\text{VLISM}}}$. Subsequently, the chi-squared estimator was calculated and its minimum value found. The fitted parameters included the absolute density of $n_{\text{He}^+_{\text{VLISM}}}$ and two instrument parameters: the conversion factor between the simulated flux and the count rate (i.e., the effective energy-independent instrument sensitivity factor), and the coefficient of reduction of instrument sensitivity for the data collected after ISN season 2012. The sensitivity of the *IBEX-Lo* instrument has been demonstrated to be very stable in time (Swaczyna et al. 2018). However, due to onboard issues the post-acceleration voltage in the electrostatic analyzer section of the instrument had to be changed in 2012. This resulted in an approximately twofold reduction of the sensitivity beginning from ISN observation season 2013. In the simulations, we assumed that the sensitivity of the instrument is a free parameter that does not depend on atom energy, and that after 2012 the instrument sensitivity is reduced by a certain factor, treated as another fitted parameter. The reduced chi-squared values obtained during the fitting process are presented in Figure 3 as a function of He^+ density in the VLISM. Transitioning from the simulated atom flux to count rates involves only linear scaling by certain factors. Consequently, fitting the two sensitivity parameters is done analytically for various simulated He^+ densities and does not require redoing the numerical modeling of the signal.

The uncertainty sources include (1) the statistical uncertainty due to the counting statistics, (2) background, (3) spin axis pointing, (4) deflection of the instrument’s optical axis from ideal alignment, (5) sensitivity to atoms with various energies, and, for the seasons 2010–2012, (6) the reduction in instrument throughput. The only important difference is that we do not need to subtract the primary ISN He population from the signal and assess the uncertainty of this subtracted signal.

The measurement uncertainty and the data covariance matrix were assessed exactly as was done by Ku2016 based on the methodology developed by Swaczyna et al. (2015). The data used in the fitting and their uncertainties are shown in Figure 4 as the red dots with error bars; note that the error bars are only approximations of the full covariance matrix of the data. The number of degrees of freedom in this study (i.e., the number of data points minus the number of fit parameters) is $N_{\text{dof}} = 1419$.

To find the best density of He^+ in the VLISM, we fit a second-order polynomial to the simulated points and the minimum of the secondary polynomial is adopted as the best estimation of the density (Figure 3). The uncertainty of the fit is obtained from the curvature of the fit and scaled to facilitate the non-canonical value of the reduced chi-squared in this study. The resulting density of He^+ in the unperturbed VLISM is obtained as $n_{\text{He}^+, \text{VLISM}} = (8.98 \pm 0.12) \times 10^{-3} \text{ cm}^{-3}$. The fitted energy-averaged sensitivity is $18.459 \times 10^{-6} \text{ cm}^2 \text{ sr}$, and the coefficient of the sensitivity drop due to post-acceleration voltage reduction is 0.4633. The uncertainty of the density $n_{\text{He}^+, \text{VLISM}}$ quoted above is solely the fit uncertainty. The best fitting model is presented along with the data with a red line in Figure 4.

The minimum chi-squared per degree of freedom (i.e., the minimum value of reduced chi-squared) obtained from the minimization is equal to 2.161, while the expected value is $1 \pm (2/N_{\text{dof}})^{1/2} = 1 \pm 0.038$. This implies that the model is not perfect. Nevertheless, the agreement between the data and our present model is better than that obtained for the model with two independent Maxwell–Boltzmann populations as in Ku2016. The chi-squared value calculated for the data set that has been updated to the identical set used with our new model by evaluating the two-Maxwellian model with the parameters of the primary ISN He from Bzowski et al. (2015) and the secondary population parameters reported by Ku2016 is 2.204 (green lines in Figure 4). Importantly, we could only minimize one parameter of the physical system, i.e., the density of He^+ , and the two parameters of the instrument sensitivity, leaving all the other parameters of the problem fixed. By contrast, in the approach adopted by Ku2016, even though the physical model was simpler than ours, the number of free parameters in the fit was larger. With a larger number of fit parameters the chi-squared values tend to decrease. In our case, we have obtained a lower chi-squared value, which suggests that the model presented in this paper is closer to the physical reality than the two-Maxwellian model used by Ku2016. Nonetheless, the systematic discrepancies between the measured and modeled count rates in the wings of later orbits during each season are generally larger for the current model than for the two-Maxwellian model. This discrepancy may suggest that the unperturbed ISN He population is not fully equilibrated and thus it may be better described by the kappa distribution far from the heliosphere instead of the Maxwell distribution (Sokół et al. 2015a; Swaczyna et al. 2019).

Figure 5 presents a comparison between the signal from our full synthesis method and the unperturbed ISN He population with the source region set to 1000 au. As evident from this comparison, the primary ISN He population observed by *IBEX* is not pristine because it has been modified by filtration. We surmise that the “filtered” portion of the signal, i.e., the negative difference between the synthesis method and the one-Maxwellian model with the filtration effects neglected, may masquerade in the comparison of data with the two-Maxwellian model as residuals that resemble patterns characteristic of a kappa distribution function of the unperturbed ISN He. More in-depth investigation of this aspect will be the subject of future studies.

To further assess the superiority of the present model over the two-Maxwellian approximation we calculated chi-squared on a subset of data where the Warm Breeze dominates. We used data from orbits 055–061, 104–109, 150a–153a, 187a–192b, and 226a–233a, a total of 756 data points. We obtained chi-squared equal to 1516.24 for the synthesis method and to 1529.75 for the two-Maxwellian model. Reduced chi-squared values were equal to 2.013 and 2.032, respectively. This suggests also that for the orbits where little of the primary population is expected, the present model fits a little better than the two-Maxwellian approximation. However, when one includes all data used in our fitting except the bins used to fit the inflow parameters of the primary population by Bzowski et al. (2015), one obtains a reduced chi-squared equal to 2.158 for the two-Maxwellian model and to 2.167 for the synthesis method. We speculate that this is because of a contribution to the data from ISN H, which was not subtracted from the data. Alternatively, it may be due to the fact that the ISN He inflow parameters we use here slightly differ from the optimum fit obtained by Bzowski et al. (2015).

The method of fitting He^+ density in the VLISM that we have used gives best results when the consistency of the model used to calculate the statistical weights ω with the global heliosphere simulation model is maintained. The quality of the fitting is very sensitive to this aspect. When in the synthesis method we assume the parameters of ISN He from Bzowski et al. (2015) instead of those from McComas et al. (2015b), but keep unchanged the parameters in the global heliosphere model (Zir2016 used the parameters from McComas et al. 2015b), then we introduce a slight inconsistency into the simulation. We assume that ISN He is flowing a little differently than the plasma at the boundary of the simulation system. From that, we obtained in the fitting the same magnitude of He^+ density (within the fit uncertainty), but a statistically significantly larger chi-squared value of 2.43, larger than in our best fit. In fact, it is larger than the chi-squared value calculated for the two-Maxwellian model with the parameters from Bzowski et al. (2015) and Ku2016. With this, the interpretation of the present model as superior to the two-Maxwellian model would not have been justified.

We consider this requirement of a high level of self-consistency in the modeling as a major strength of our approach and the result. While the inferred density of He^+ is model-dependent, the model we used is self-consistent. Consequently, it is not advisable to modify one of its aspects (e.g., heliopause location; *B*-field direction or strength; allowing for kappa distribution functions for the plasma or ISN He; tensor-like thermal spread of the plasma or ISN gas, etc.) without propagating it self-consistently into the global

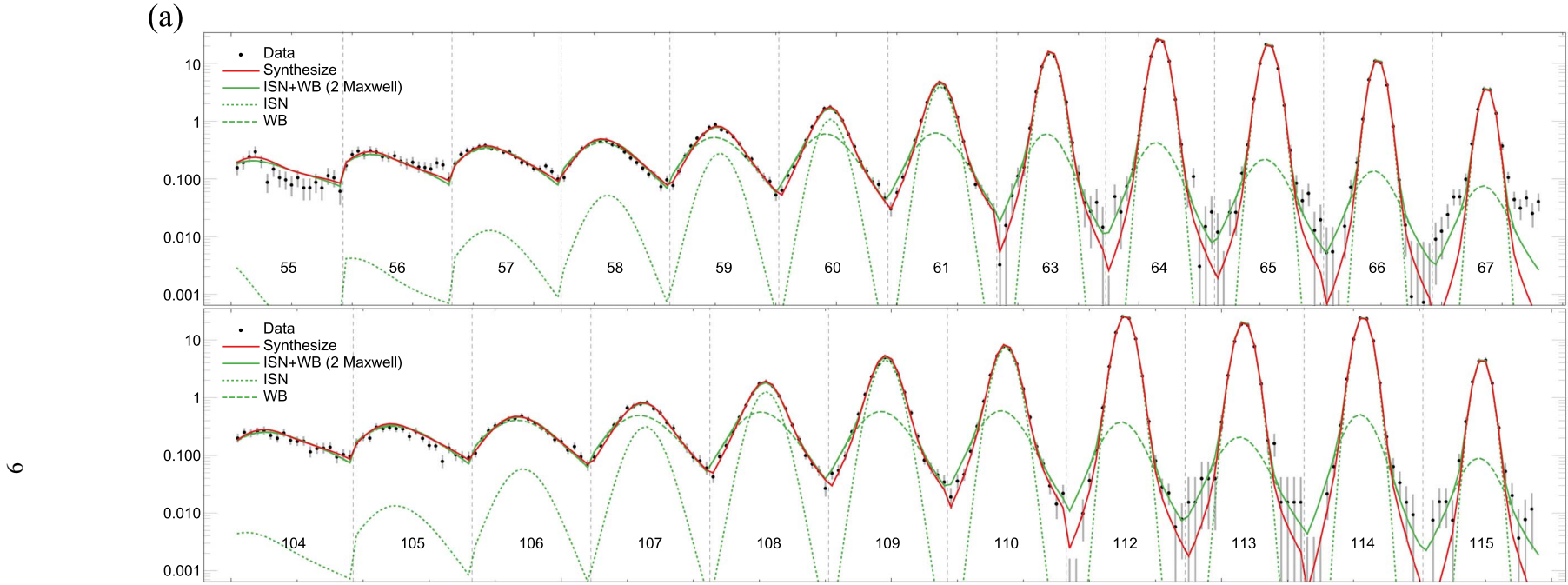


Figure 4. Orbit-averaged count rates observed by *IBEX*-Lo and their uncertainties (black points with error bars), compared with the model obtained in this paper (red line) and the best fitting model obtained by [Ku2016](#) assuming that the primary and Warm Breeze (secondary) populations of ISN He are given by independent, homogeneous Maxwell–Boltzmann distribution functions in the VLISM (solid green lines). For comparison, the primary ISN He and the Warm Breeze populations from the two-Maxwellian models are shown (dotted and dashed green lines, respectively). Each panel corresponds to one observation season: 2010–2014, from top to bottom. The labels in the panels between the vertical bars indicate the reference numbers of the *IBEX* orbital arcs. The data between the bars are arranged by *IBEX* spin angle; the data cover the spin angle range from 222° to 312° .

10

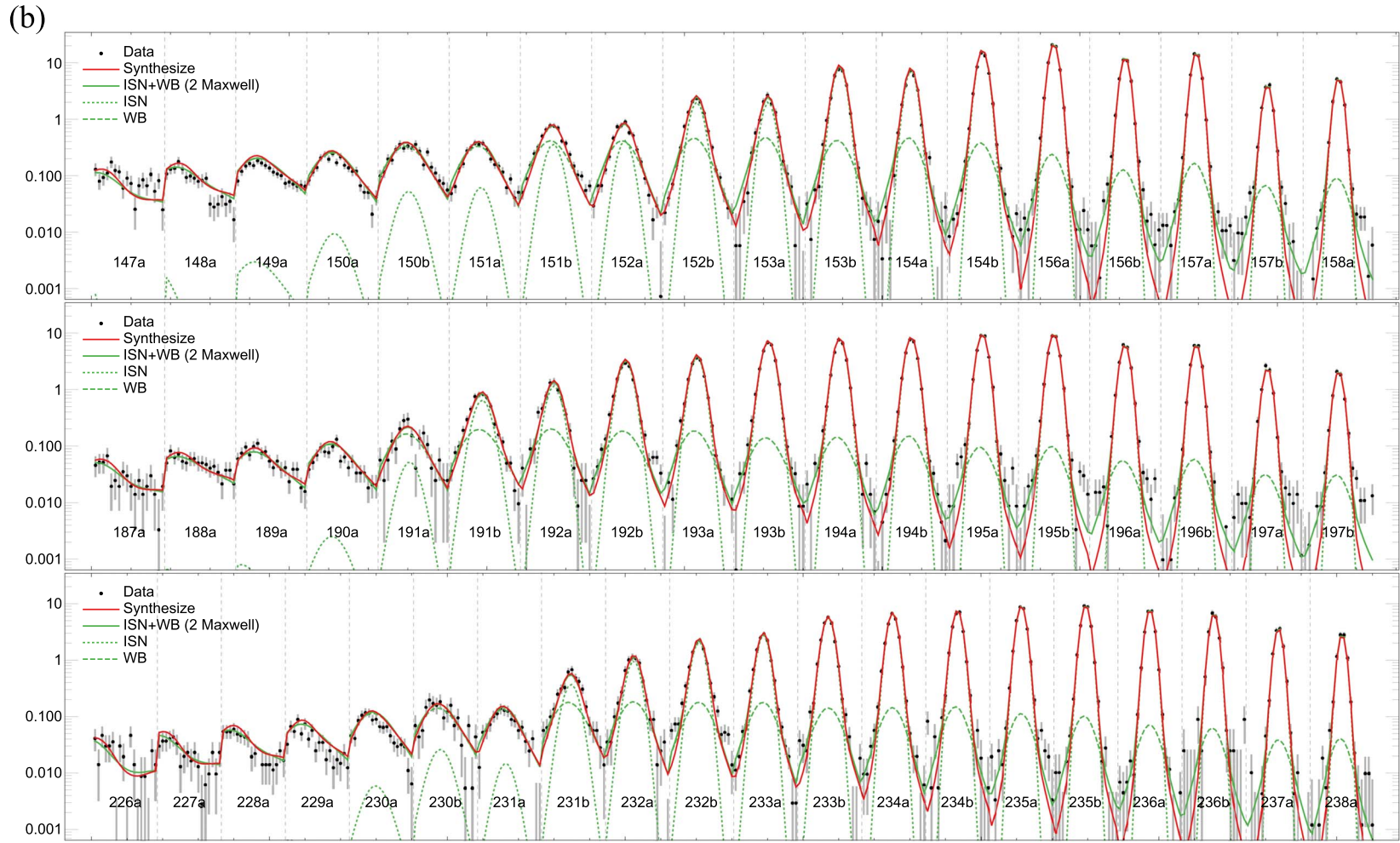


Figure 4. (Continued.)

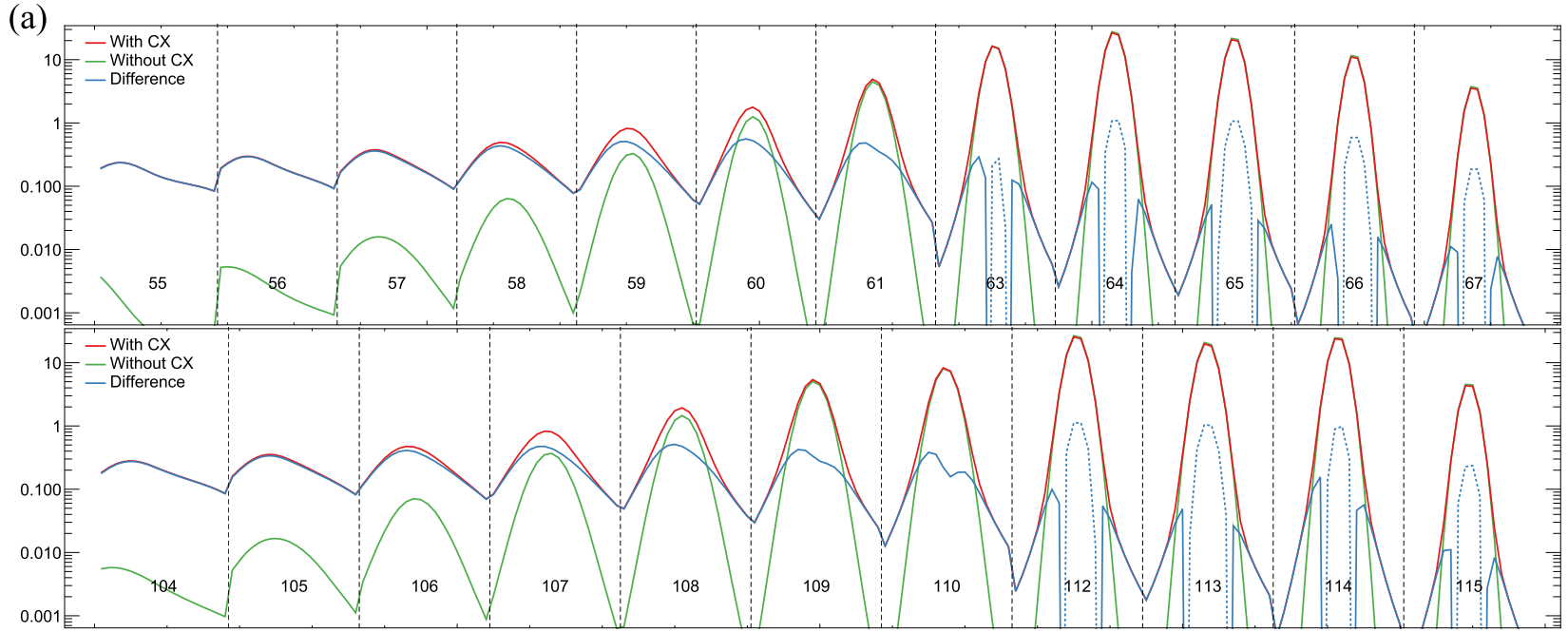


Figure 5. Illustration of the filtration of the primary ISN He population in the OHS. The red line marks the result of the synthesis method, copied from Figure 4. The green line is the primary population signal obtained assuming that there are no charge exchange processes operating in the OHS. The blue line shows the difference between these two signals. The dotted line indicates when this difference is negative. A negative difference implies that ISN atoms have been filtered out from the original unperturbed population.

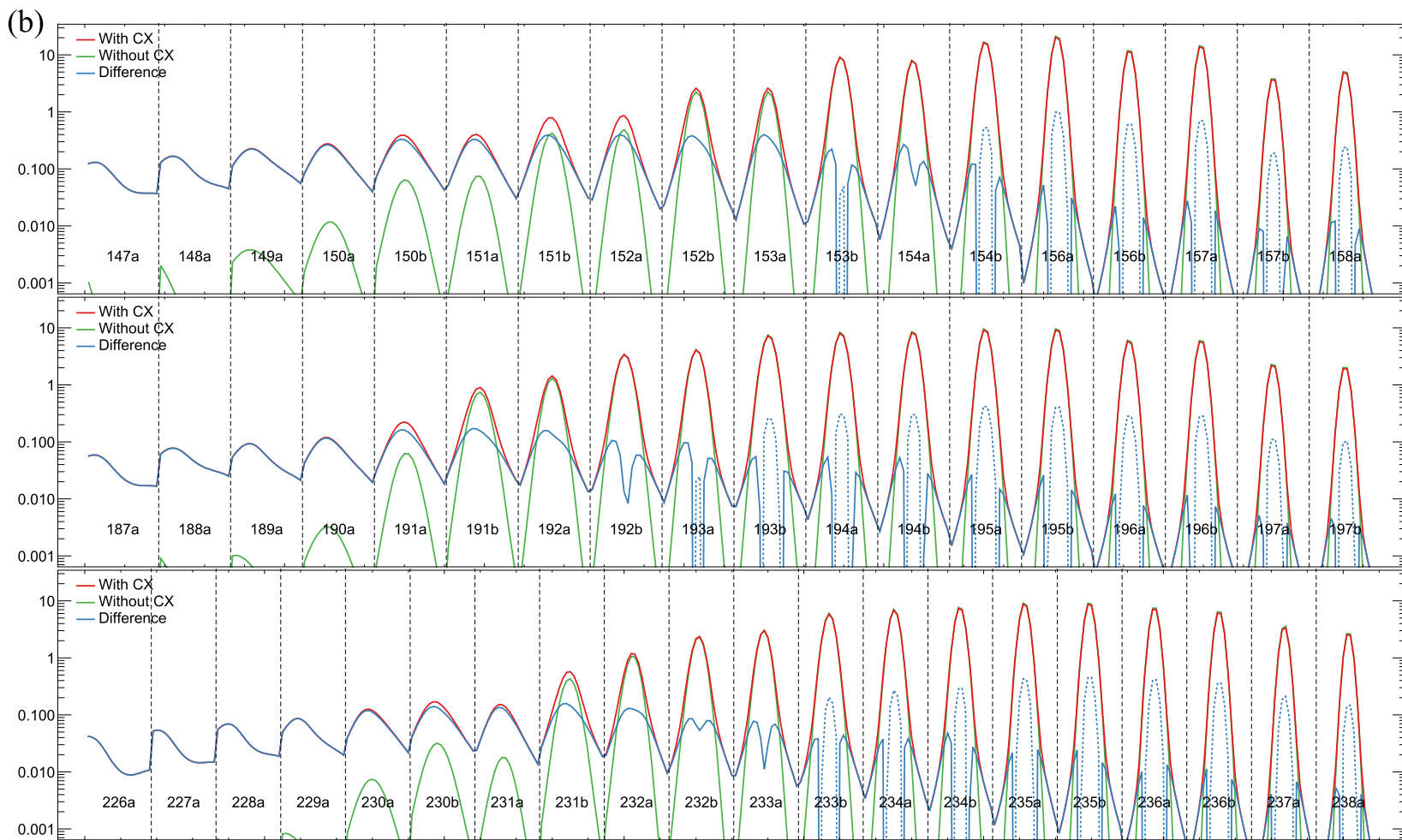


Figure 5. (Continued.)

heliosphere model and the statistical weight calculation. This makes it a suitable tool for verifying predictions of various global heliosphere models against observations, with different approximations made or different parameters used.

6. Derivation of VLISM Parameters

Using the density of the interstellar He^+ component obtained from fitting and with the model parameters listed in Table 1, we derive other parameters of the VLISM as follows. To calculate the proton density, we do not need to assume the frequently used cosmological He/H abundance because, having all relevant quantities measured, we do not need to pre-assume anything in this respect. Generally, the cosmological abundance is not a reliable estimate for the local He/H abundance because of different chemical processing of matter in various populations of stars and its subsequent redistribution by supernova explosions in different regions of space (e.g., Wilson & Rood 1994). In particular, the Local Bubble and the local interstellar medium very likely were heavily processed by a series of supernova explosions a few million years ago (Breitschwerdt et al. 1996). With the mass density of the VLISM plasma

$$\rho_{\text{pl}} = (n_{\text{H}^+} + 4 n_{\text{He}^+}) m_{\text{nuc}} \quad (11)$$

we calculate

$$n_{\text{H}^+} = \rho_{\text{pl}} / m_{\text{nuc}} - 4 n_{\text{He}^+}. \quad (12)$$

The electron density in the VLISM is given by

$$n_e = n_{\text{H}^+} + n_{\text{He}^+}, \quad (13)$$

the ionization degree of He in the VLISM is equal to

$$X_{\text{He}} = n_{\text{He}^+} / (n_{\text{He}^+} + n_{\text{He}}), \quad (14)$$

and the ionization degree of ISN H is obtained as

$$X_{\text{H}} = n_{\text{H}^+} / (n_{\text{H}} + n_{\text{H}^+}). \quad (15)$$

Numerical values for these parameters are listed in Table 2. The densities of the ionized components we have obtained do not imply a deviation from the cosmological H/He ratio larger than $\sim 15\%$.

7. Discussion and Conclusions

The data we have used were collected between 2009 November and 2014 March, over a time span of ~ 4.5 yr (with gaps of eight months in measurements each year). The speed of the Sun's motion relative to the VLISM is 25.4 km s^{-1} , i.e., 5.36 au yr^{-1} ; thus, during the measurement interval the Sun has covered less than $23 \text{ au} = 1.1 \times 10^{-4} \text{ pc}$ relative to this matter, which is at least five orders of magnitude less than the expected size of the cloud of interstellar matter the Sun is traveling through. In the determination of magnetic field performed by Zir2016 based on fitting the Ribbon size and location in the sky, the ENA signal originates within ~ 500 au from the Sun (see Figure 1 in their paper), i.e., $2.5 \times 10^{-3} \text{ pc}$. Therefore, from the perspective of the size of a parsec, typical for interstellar clouds in the Sun's neighborhood, the result of this analysis can be regarded as a point measurement of the plasma condition in the VLISM.

Slavin & Frisch (2008) performed a parametric study of the VLISM conditions based on radiative transfer calculations and the data available back then, in particular for the previously

thought VLISM temperature of 6300 K. The goal was to match the available data on the Local Interstellar Cloud (LIC) including column densities of several ions based on absorption lines and in situ data such as the neutral He density. This was done by constructing the ionizing radiation field based on (1) directly observed nearby hot stars and (2) modeled emission from hot gas in the LB (responsible for the diffuse soft X-ray background, McCammon et al. 1983; Snowden et al. 1997). An additional component to the radiation field from a hypothesized evaporative boundary to the LIC was also modeled and included. The radiation field was transferred through the cloud to the location of the Sun using the radiative transfer/thermal equilibrium code Cloudy (Ferland et al. 2013). Various parameters, such as elemental abundances and the density, and the magnetic field in the cloud, were then varied to achieve good matches to the data.

Slavin & Frisch (2008) explored a large grid of parameters (42, see their Table 2 for the input values and Table 4 for the results), and they isolated several of the most promising sets. Since then, estimates for the VLISM temperature have increased to ~ 7500 K and the strength of magnetic field has been better constrained ($\sim 3 \mu\text{G}$). It has also become clear that a fraction of the emission in the soft X-ray diffuse background originates within the heliosphere, generated by charge exchange between inflowing neutrals and solar wind ions (Snowden 2015). As a result, the intensity of the EUV/X-ray emission from the hot gas of the LB was overestimated in Slavin & Frisch (2008). Recent estimates of the fraction of the soft X-ray emission coming from the LB near the Galactic plane range from 26% (Smith et al. 2014) to 60% (Galeazzi et al. 2014). The Cloudy code has also been improved in the intervening years.

Given these changes, we have recalculated the ionization of the LIC for several parameter sets. The major assumed parameters in this modeling are the temperature of the hot gas in the LB and the opacity of the cloud, which depends on the column density. The density and magnetic field of the cloud were varied to achieve the desired values for the neutral He density and temperature at the heliosphere. In addition, we have looked at different fractions of the soft X-rays that come from the LB. Since the soft X-ray background is brightest out of the Galactic plane, the fractions mentioned above are lower limits. For an assumed fraction of 75%, an LB temperature of 10^6 K, and cloud column density of $N(\text{H I}) = 4 \times 10^{17} \text{ cm}^{-2}$, we found that we need a magnetic field of $3.5 \mu\text{G}$. The values found for ionization then are $X_{\text{H}^+} = 0.245$, $X_{\text{He}^+} = 0.395$, $n_{\text{H}^+} = 6.2 \times 10^{-2} \text{ cm}^{-3}$, $n_{\text{He}^+} = 9.9 \times 10^{-3} \text{ cm}^{-3}$, and $n_e = 7.2 \times 10^{-2} \text{ cm}^{-3}$. Using 50% for the soft X-ray fraction yields similar results but requires a higher magnetic field, $B = 4 \mu\text{G}$. These results had been generated before the currently reported *IBEX-Lo* results were available.

Wolff et al. (1999), based on *EUVE* observations of nearby white dwarfs, compared column densities of H, He, and He^+ in the local interstellar medium and found that the ionization degree of He is 0.4 (with a large uncertainty), consistent with our value of 0.37, and the He^+/H ratio they obtained is 0.052 ± 0.007 , in agreement with our 0.056–0.058. This suggests that the properties of VLISM obtained independently from astrophysical and heliospheric observations converge.

Discriminating between alternative VLISM parameter sets solely with the use of radiative transfer calculations and telescopic observations seems challenging. Our analysis

suggests that observations of ISN He can help in this discrimination. Our fitting the ISN He observations from *IBEX*-Lo resulted in assessments of $8.98 \times 10^{-3} \text{ cm}^{-3}$ for the density of He^+ , $5.41 \times 10^{-2} \text{ cm}^{-3}$ for the proton density, $6.30 \times 10^{-2} \text{ cm}^{-3}$ for the electron density, and 0.26 and 0.37 for the ionization degrees of H and He, respectively. These are in very good agreement with the aforementioned estimates based on equilibrium models of the VLISM. This agreement lends credence to the consistency of the global heliosphere model and the physical state of the VLISM.

M.B., A.C., and E.J.Z. gratefully acknowledge the collaboration within ISSI Team 368 The Physics of the Very Local Interstellar Medium and its interaction with the heliosphere. The work at CBK PAN was supported by the Polish National Science Centre grants 2015/18/M/ST9/00036 and 2015/19/B/ST9/01328. J.H. and E.J.Z. acknowledge support from NASA grant 80NSSC18K1212. The US portion of this work was funded by the *IBEX* mission as a part of the NASA Explorer Program (NNG17FC93C; NNX17AB04G). E.J.Z. also acknowledges partial support from NASA grant 80NSSC17K0597. A.G. and P.W. were supported by the Swiss national Science Foundation.

ORCID iDs

M. Bzowski  <https://orcid.org/0000-0003-3957-2359>
 A. Czechowski  <https://orcid.org/0000-0002-4441-5377>
 A. Galli  <https://orcid.org/0000-0003-2425-3793>
 J. Grygorczuk  <https://orcid.org/0000-0003-3951-0043>
 J. Heerikhuisen  <https://orcid.org/0000-0001-7867-3633>
 M. A. Kubiak  <https://orcid.org/0000-0002-5204-9645>
 D. J. McComas  <https://orcid.org/0000-0002-9745-3502>
 E. Möbius  <https://orcid.org/0000-0002-2745-6978>
 N. A. Schwadron  <https://orcid.org/0000-0002-3737-9283>
 J. Slavin  <https://orcid.org/0000-0002-7597-6935>
 J. M. Sokół  <https://orcid.org/0000-0002-4173-3601>
 P. Swaczyna  <https://orcid.org/0000-0002-9033-0809>
 P. Wurz  <https://orcid.org/0000-0002-2603-1169>
 E. J. Zirnstein  <https://orcid.org/0000-0001-7240-0618>

References

- Adams, T. F., & Frisch, P. C. 1977, *ApJ*, 212, 300
 Baranov, V. B., & Malama, Y. G. 1993, *JGR*, 98, 15157
 Barnett, C. F., Hunter, H. T., Kirkpatrick, M. I., et al. 1990, Atomic Data for Fusion. Collisions of H, H₂, He and Li Atoms and Ions with Atoms and Molecules, Vol. ORNL-6086/V1 (Oak Ridge, TN: Oak Ridge National Laboratories)
 Bloch, J. J., Jahoda, K., Juda, M., et al. 1986, *ApJL*, 308, L59
 Breitschwerdt, D., Egger, R., Freyberg, M. J., Frisch, P. C., & Vallerger, J. V. 1996, *SSRv*, 78, 183
 Burlaga, L. F., & Ness, N. F. 2016, *ApJ*, 829, 134
 Bzowski, M., Kubiak, M. A., Czechowski, A., & Grygorczuk, J. 2017, *ApJ*, 845, 15
 Bzowski, M., Kubiak, M. A., Hlond, M., et al. 2014, *A&A*, 569, A8
 Bzowski, M., Kubiak, M. A., Möbius, E., et al. 2012, *ApJS*, 198, 12
 Bzowski, M., Möbius, E., Tarnopolski, S., Izmodenov, V., & Gloeckler, G. 2008, *A&A*, 491, 7
 Bzowski, M., Möbius, E., Tarnopolski, S., Izmodenov, V., & Gloeckler, G. 2009, *SSRv*, 143, 177
 Bzowski, M., Sokół, J. M., Kubiak, M. A., & Kucharek, H. 2013a, *A&A*, 557, A50
 Bzowski, M., Sokół, J. M., & Tokumaru, M. 2013b, in Cross-Calibration of Past and Present Far UV Spectra of Solar System Objects and the Heliosphere, ed. R. M. Bonnet, E. Quemerais, & M. Snow (Berlin: Springer), 67
 Bzowski, M., Swaczyna, P., Kubiak, M., et al. 2015, *ApJS*, 220, 28
 Crutcher, R. M. 1982, *ApJ*, 254, 82
 Cummings, A. C., Stone, E. C., & Steenberg, C. D. 2002, *ApJ*, 578, 194
 Fahr, H. J., & Mueller, K. G. 1967, *ZPhy*, 200, 343
 Fahr, H. J., & Ruciński, D. 1999, *A&A*, 350, 1071
 Ferland, G. J., Porter, R. L., van Hoof, P. A. M., et al. 2013, *RMxAA*, 49, 137
 Frisch, P. C., Berdyugin, A., Piirola, V., et al. 2015, *ApJ*, 814, 112
 Frisch, P. C., Grodnicki, L., & Welty, D. E. 2002, *ApJ*, 574, 834
 Frisch, P. C., Redfield, S., & Slavin, J. D. 2011, *ARA&A*, 49, 237
 Funsten, H. O., DeMajistre, R., Frisch, P. C., et al. 2013, *ApJ*, 776, 30
 Fuselier, S. A., Bochsler, P., Chornay, D., et al. 2009, *SSRv*, 146, 117
 Galeazzi, M., Chiao, M., Collier, M. R., et al. 2014, *Natur*, 512, 171
 Galli, A., Wurz, P., Park, J., et al. 2015, *ApJS*, 220, 30
 Galli, A., Wurz, P., Rahmaniard, F., et al. 2019, *ApJ*, 871, 52
 Galli, A., Wurz, P., Schwadron, N., et al. 2016, *ApJ*, 821, 107
 Gloeckler, G., Allegrini, F., Elliott, H. A., et al. 2004, *ApJL*, 604, L121
 Gloeckler, G., & Geiss, J. 2001, *SSRv*, 97, 169
 Gry, C., & Jenkins, E. B. 2014, *A&A*, 567, A58
 Grygorczuk, J., Ratkiewicz, R., Strumik, M., & Grzedziński, S. 2011, *ApJL*, 727, L48
 Gurnett, D. A., Kurth, W. S., Burlaga, L. F., & Ness, N. F. 2013, *Sci*, 341, 1489
 Gurnett, D. A., Kurth, W. S., Stone, E. C., et al. 2015, *ApJ*, 809, 121
 Heerikhuisen, J., & Pogorelov, N. V. 2010, in ASP Conf. Ser. 429, Numerical Modeling of Space Plasma Flows, Astronom-2009, ed. N. V. Pogorelov, E. Audit, & G. P. Zank (San Francisco, CA: ASP), 227
 Heerikhuisen, J., & Pogorelov, N. V. 2011, *ApJ*, 738, 29
 Heerikhuisen, J., Pogorelov, N. V., Zank, G. P., et al. 2010, *ApJL*, 708, L126
 Heerikhuisen, J., Zirnstein, E., & Pogorelov, N. 2015, *JGR*, 120, 1516
 Heerikhuisen, J., Zirnstein, E. J., Pogorelov, N. V., Zank, G. P., & Desai, M. 2019, *ApJ*, 874, 76
 Isenberg, P. A. 1986, *JGR*, 91, 9965
 Izmodenov, V., Gloeckler, G., & Malama, Y. 2003a, *GeoRL*, 30, 3
 Izmodenov, V., Malama, Y. G., Gloeckler, G., & Geiss, J. 2003b, *ApJL*, 594, L59
 Izmodenov, V. V., & Alexashov, D. B. 2015, *ApJS*, 220, 32
 King, J. H., & Papitashvili, N. E. 2005, *JGR*, 110, 2104
 Kowalska-Leszczynska, I., Bzowski, M., Sokół, J. M., & Kubiak, M. A. 2018, *ApJ*, 868, 49
 Kubiak, M. A., Bzowski, M., Sokół, J. M., et al. 2014, *ApJS*, 213, 29
 Kubiak, M. A., Swaczyna, P., Bzowski, M., et al. 2016, *ApJS*, 223, 35
 Lallement, R., Quémerais, E., Bertaux, J. L., et al. 2005, *Sci*, 307, 1447
 Lee, M. A., Fahr, H. J., Kucharek, H., et al. 2009, *SSRv*, 146, 275
 McComas, D., Burrows, D. N., Sanders, W. T., & Kraushaar, W. L. 1983, *ApJ*, 269, 107
 McComas, D., Bzowski, M., Frisch, P., et al. 2015a, *ApJ*, 801, 28
 McComas, D., Bzowski, M., Fuselier, S., et al. 2015b, *ApJS*, 220, 22
 McComas, D. J., Allegrini, F., Bochsler, P., et al. 2009, *SSRv*, 146, 11
 McComas, D. J., Angold, N., Elliott, H. A., et al. 2013, *ApJ*, 779, 2
 McComas, D. J., Ebert, R. W., Elliot, H. A., et al. 2008, *GeoRL*, 35, L18103
 Möbius, E., Bochsler, P., Bzowski, M., et al. 2009a, *Sci*, 326, 969
 Möbius, E., Bochsler, P., Heirtzler, D., et al. 2012, *ApJS*, 198, 11
 Möbius, E., Bzowski, M., Chalov, S., et al. 2004, *A&A*, 426, 897
 Möbius, E., Bzowski, M., Fuselier, S. A., et al. 2015, *ApJS*, 220, 24
 Möbius, E., Kucharek, H., Clark, G., et al. 2009b, *SSRv*, 146, 149
 Pogorelov, N. V., Heerikhuisen, J., Mitchell, J. J., Cairns, I. H., & Zank, G. P. 2009, *ApJL*, 695, L31
 Pogorelov, N. V., Heerikhuisen, J., & Zank, G. P. 2008, *ApJL*, 675, L41
 Redfield, S., & Linsky, J. L. 2008, *ApJ*, 673, 283
 Richardson, J. D. 2008, *GeoRL*, 35, 23104
 Richardson, J. D., Liu, Y., Wang, C., & McComas, D. 2008, *A&A*, 491, 1
 Schwadron, N., Möbius, E., Leonard, T., et al. 2015, *ApJS*, 220, 25
 Schwadron, N. A., Möbius, E., McComas, D. J., et al. 2016, *ApJ*, 828, 81
 Slavin, J. D., & Frisch, P. C. 2008, *A&A*, 491, 53
 Smith, R. K., Foster, A. R., Edgar, R. J., & Brickhouse, N. S. 2014, *ApJ*, 787, 77
 Snowden, S. L. 2015, *Journal of Physics: Conference Series*, 577, 012022
 Snowden, S. L., Egger, R., Freyberg, M. J., et al. 1997, *ApJ*, 485, 125
 Sokół, J. M., & Bzowski, M. 2014, arXiv:1411.4826
 Sokół, J. M., Bzowski, M., Kubiak, M., et al. 2015a, *ApJS*, 220, 29
 Sokół, J. M., Bzowski, M., & Tokumaru, M. 2019, *ApJ*, 872, 57

- Sokół, J. M., Kubiak, M., Bzowski, M., & Swaczyna, P. 2015b, [ApJS](#), **220**, 27
- Stone, E. C., Cummings, A. C., McDonald, F. B., et al. 2013, [Sci](#), **341**, 150
- Swaczyna, P., Bzowski, M., Kubiak, M., et al. 2015, [ApJS](#), **220**, 26
- Swaczyna, P., Bzowski, M., Kubiak, M., et al. 2018, [ApJ](#), **854**, 119
- Swaczyna, P., McComas, D., & Schwadron, N. 2019, [ApJ](#), **871**, 254
- Tokumaru, M., Fujiki, K., & Iju, T. 2015, [JGR](#), **120**, 3283
- Vallerga, J., Lallement, R., Lemoine, M., Dalaudier, F., & McMullin, D. 2004, [A&A](#), **426**, 855
- Wilson, T. L., & Rood, R. 1994, [ARA&A](#), **32**, 191
- Witte, M. 2004, [A&A](#), **426**, 835
- Wolff, B., Koester, D., & Lallement, R. 1999, [A&A](#), **346**, 969
- Wood, B. E., Müller, H.-R., & Witte, M. 2015, [ApJ](#), **801**, 62
- Zirnstein, E. J., Heerikhuisen, J., Funsten, H. O., et al. 2016, [ApJL](#), **818**, L18